Origin of Visible Light Photoactivity of the CeO2/ZnO Heterojunction

Origin of Visible Light Photo-Activity of the CeO_2/ZnO Hetero-Junction

Erik Cerrato[¥], Chiara Gionco[¥], Maria Cristina Paganini[¥], Elio Giamello[¥] *, Elisa Albanese[¤], Gianfranco Pacchioni[¤]

[¥] Dipartimento di Chimica and NIS, Università di Torino, Via P. Giuria 7, 10125 Torino, ITALY

[¤] Dipartimento di Scienza dei Materiali, Università di Milano Bicocca, Via R. Cozzi 55, 20125 Milano, ITALY

*Elio Giamello: elio.giamello@unito.it, Via Giuria 7, 10125 Torino, +39-011-6707574

Abstract: The synthesis of a mixed CeO_2-ZnO oxide results in a photo-catalyst active under visible light. The characterization of the new material shows that Ce does not enter as a dopant in ZnO but rather forms isolated CeO_2 nanoparticles supported on the surface of larger particles of the more abundant zinc oxide phase. The as obtained material exhibits a band gap corresponding to UV light (≈3.3 eV), but nevertheless it shows a relevant photo-activity under irradiation with photons with $\lambda > 420$ nm (visible light). The working hypothesis is that visible light irradiation leads to a charge separation and stabilisation of a fraction of the carriers connected with the formation of the CeO_2/ZnO interface. This phenomenon has been investigated by means of several methods. A specific EPR-based approach allowed to monitor and quantify the charge separation following the formation of holes in the valence band (VB) of the two materials. More complex is detecting the nature of the excited electrons, as this involves the formation of EPR invisible Ce^{3+} ions by trapping the electrons into localized 4f states of Ce ions at the interface between the two oxides. DFT calculations provide a rational for some of the observed phenomena, and a basis for the discussion of the band alignment of the two systems as a consequence of the formation of a hetero-junction. The theoretical results show that indeed electrons can be excited at the interface from the VB of the two oxides into the Ce 4f states with photons of 2.3 eV, thus justifying the occurrence of a visible-light activity despite the higher band gap of the two materials.

1. Introduction

The increasing awareness concerning climate change and the need to drastically reduce the use of fossil fuels has generated an intense debate among nations that have led to specific agreements and future objectives [1, 2]. Much before the definition of international agreements, the scientific community began to be involved in the development of alternative energy systems aimed to overcome the systematic use of fossil fuels. Chemistry and Material Science research started long ago to be attracted by the use of solar energy either for the production of electricity or to provide the energy supply needed by various chemical processes. In the latter case, the advent of photocatalytic processes is exemplary. Photocatalysis is used for various purposes including: i) production of solar fuels either by water photo-splitting or by CO_2 reduction processes (artificial photosynthesis, APS [3]), ii) pollutants remediation in water and atmosphere (environmental photocatalysis [4]), iii) the achievement of alternative routes to traditional synthetic processes in organic chemistry [5, 6]. Oxide-based systems play a major role in all the mentioned areas. The first seminal experiment in APS dates back to 1972 when A. Fujshima reported the photo-assisted water electrolysis employing a titanium dioxide film as a photoanode for water oxidation to O_2 [7]. TiO_2 later became (and still remains) the reference system for environmental photocatalysis reactions in which the optimal oxidation potential of the holes, formed in the valence band (VB) by photoexcitation of electrons, is exploited for the mineralization of pollutants.

Over the years, however, two non-negligible limitations of titanium dioxide as a photocatalyst have emerged. These are: i) the weak reductive potential of photoexcited electrons in the conduction band (CB) of the solid, and ii) the amplitude of the band gap of the oxide, which makes UV light necessary for the VB to CB electron excitation. If the latter limit is not a problem for laboratory reactions, it becomes important for large scale plants aiming to use sunlight. The ultraviolet component with photon energy higher than 3.2 eV (TiO_2 energy gap, corresponding to ca. 390 nm) in sunlight is about 4%. These limitations stimulated the search for new systems capable of exploiting visible light in all photocatalytic phenomena.

The search for new oxide-based semiconductors (oxides are generally robust, corrosion resistant, and cheap) to be used in energetic (APS) and environmental applications of photocatalysis [8, 9] has become compelling as, in particular for hydrogen production, a competitive solution in terms of cost with methane reforming is not currently available. Our research groups have been active for more than a decade in the study of photoactive materials capable of combining good redox potential and

visible light sensitivity. These two apparently irreconcilable goals can be addressed either by exploring the vast family of metal oxides and related compounds [10], or by modifying relatively common oxides by chemical methods enabling the onset of photo-activity in the visible. Representative of this route is the nitrogen-doped titanium dioxide system (N/TiO_2) introduced by Asahi in 2001 [11] which, though it did not achieve the initial expectations, remains a reference system in conceptual terms and for some applications in environmental photocatalysis.

More recently, our and other [12-14] research groups started to investigate the role of cerium as dopant of oxides. The Ce/ZrO_2 system, zirconium dioxide containing Ce^{4+} ions (from 0.5% to 10%) diluted in the oxide lattice, proved to be a system photoactive under visible light irradiation [15]. In our approach, the photoactivity is preliminarily investigated monitoring the charge separation under different irradiation conditions and using Electron Paramagnetic Resonance (EPR) to identify the photogenerated carriers stabilized in the solid or at its surface [16, 17]. Pristine ZrO_2 exhibits an energy gap of more than 5 eV and, thus, it is impossible to use visible (or even solar light) for charge separation. The observed photoactivity of Ce/ZrO_2 is due to the presence of Ce^{4+} (empty) 4f states approximately located in the middle of the band gap which are able to host electrons excited from the VB by visible light photons [12, 18]. Despite the fact that some Ce/ZrO_2 materials have shown an interesting activity in pollutants remediation [15], this system still represents a proof of concept. Different features from those described above have been shown by CeO_2-ZnO-based materials, the object of this paper. In this case, in fact, cerium ions are not soluble in the ZnO matrix. Mixing, using a wet chemistry approach, the cerium with the zinc components, results in small particles of CeO_2 at the surface of the more abundant zinc oxide phase. This composite system has shown an amazing, unexpected activity in the mineralization of acelsulfame K, a so-called emerging pollutant, performed under visible light [19]. This result led us to an in-depth study of the new material. This is reported in the present paper which is organized as follows. First, the preparation of the solid and its structural and morphological features are described. Second, the photochemical properties are investigated using various kinds of irradiation and adopting the previously described EPR-bases approach to monitor the charge separation and stabilization. All these results, as shown in the past for other photoactive systems [12, 20, 21], can be strongly reinforced by a careful modelling of the electronic structure of the solid by computational methods. A thorough understanding of the mechanism operating in the solid under irradiation with different types of light needs in fact a detailed knowledge of the energy levels present in the mixed solid. In the present case, this has been particularly challenging since the CeO_2/ZnO system is biphasic and the role of the solid-solid

interface has to be taken into consideration. As it will be shown below, it is indeed the role of these interfaces (or heterojunctions) that allows a better understanding of this novel promising photocatalytic system.

2. Materials and Methods

2.1 Samples preparation

All reactants employed in this work were obtained from Sigma Aldrich and used without any further purification treatment. The samples have been prepared via a precipitation method using $Zn(CH_3COO)_2 \bullet 2H_2O$ (90.0%) and $CeCl_3$ (99,99%)$\bullet 7H_2O$ as starting material and dopant source, respectively. The undoped ZnO was synthetized dissolving 2.2 g of $Zn(CH_3COO)_2 \bullet 2H_2O$ into 160 ml of distilled water; 80 ml of ethanol was added to the solution and stirred for 1 hour; then 160 ml of a NaOH aqueous solution 1M was added, always stirring, at room temperature. The precipitate, after 48 hours, was separated via filtration, washed with distilled water, and dried at 70°C for 12 hours [22]. The final product was obtained after calcination at 300°C for 30 hours in air. The bare sample will be indicated as ZnO. The doped sample containing 1% mol of Ce was synthetized adding 0.038 g of $CeCl_3 \bullet 7H_2O$ to the starting mixture. It will be labelled with CZ1.

All the experiments reported in Section 3.3 were performed on activated samples. The as prepared materials were activated, in order to eliminate hydroxyl and carboxyl groups from the surface and to obtain a material as close as possible to the expected stoichiometry, by thermal annealing under vacuum at 570K (30 min). This treatment was followed by oxidation in oxygen atmosphere (50 mbar) at 670K.

2.2 Samples characterization

All samples were characterized via X-ray diffraction (XRD), N_2 adsorption to evaluate surface area (BET method), diffuse reflectance UV-Vis spectroscopy, transmission electron microscopy (TEM), and electron paramagnetic resonance (EPR).

Powder X-rays diffraction (XRD) patterns of the as prepared samples were recorded with a PANalytical PW3040/60 X'Pert PRO MPD using a copper K_α radiation source (0.154056 nm). The signals were scanned continuously in the 2θ ranges between 20° and 80°. In order to identify the phases, present in the samples, the X'Pert High-Score software was used. Scherrer refinement was performed on the diffraction patterns to define the crystallite size of the existing phases.

The specific surface area measurements were carried out on a Micromeritics ASAP 2020 using the Brunauer-Emmett-Teller (BET) model on the N_2 adsorption measurement. Prior to the adsorption run, all the samples were outgassed at 573 K for two hours.

The UV-Vis absorption spectra were recorded using a Varian Cary 5 spectrometer, equipped with an integration sphere for diffuse reflectance studies, using a Carywin-UV/scan software. A sample of Teflon with 100% reflectance was used as reference.

The optical band gap energies were calculated considering that the energy dependence of the absorption coefficient (α) for semiconductors in the region near the absorption edge is given by:

$$\alpha \propto \frac{(h\nu - E_{bg})^{\eta}}{h\nu}$$

Where hν is the energy of the incident photon and E_{bg} is the optical absorption energy. η depends on the type of optical transition, in crystalline semiconductors is 1/2 (direct-allowed), 3/2 (direct-forbidden), 2 (indirect-allowed), and 3 (indirect-forbidden). For what concerns ZnO and CeO_2, they show a direct-allowed optical transition, with a value of 1/2 for η. Finally, since the scattering coefficient weakly depends on energy and $F(R_\infty)$, it can be assumed as proportional to the absorption coefficient within the narrow range of energy containing the absorption edge feature.

$$F(R_\infty) = \frac{(h\nu - E_{bg})^{\eta}}{h\nu}$$

Then, the plot $(F(R_\infty)*h\nu)^{1/\eta}$ vs hν can be used to determine the absorption edge energy (Tauc plot) method.

In this way the energy gaps were calculated and reported in table 1.

The TEM images were achieved with a high-resolution transmission electron microscope (HRTEM) using a JEOL JEM 3010UHR (300 kV); samples were dry deposited on Cu “holey” carbon grids. The TEM instrument was equipped with an Energy Dispersive Spectroscopy (EDS) probe.

The Electron Paramagnetic Resonance spectra was recorded both at room temperature and at liquid nitrogen temperature (77 K) using a X-band CW-EPR Bruker EMX spectrometer equipped with a cylindrical cavity operating at 100 KHz field modulation. The effect of light on EPR spectra was investigated using a 1000 W Xenon lamp (Oriel Instruments) equipped with an IR water filter. To investigate the effect of visible light on the materials different cut-off filters (Newport-20CGA) at 400, 420, 455 and 495 nm have been used for selected experiments: this kind of filters offer a good coverage with a range of ±10 nm. The lamp provides a constant photon flow from 250 nm to 750 nm. Using these cut-off filters, the photon flow is reduced by about one third. Computer simulation

of the EPR spectra were obtained using the SIM32 program developed by Prof. Sojka (Jagellonian University, Cracow, Poland) [23].

2.3. Computational Details

All calculations were carried out using the Heyd-Scuseria-Ernzerhof (HSE) hybrid functional [24-26], as implemented in CRYSTAL14 code [27]. This short-range hybrid DFT functional is indeed able to accurately reproduce band gap and band alignment of several oxides [28].

Crystalline orbitals are represented as linear combinations of Bloch functions (BF) and are evaluated over a regular three-dimensions mesh of points in reciprocal space. Each BF is built from local atomic orbitals (AO) resulting from contractions of Gaussian-type-functions, which in turn are the product of a Gaussian times a real solid spherical harmonic function. All electron basis sets have been adopted for O, and Zn. For Ce an ECP has been used [29], and the electrons explicitly treated are $4s^2 4p^6 4d^{10} 5s^2 5p^6 4f^1 6s^2 5d^1$, with a (10sp7d8f)/[4sp2d3f] basis set properly optimized [30]. In ZnO slab calculations, a layer of atomic ghost functions has been added to ensure the correct description of the electron density at the oxide/vacuum interface.

For the numerical integration of exchange-correlation term, 75 radial points and 974 angular points (XLGRID) in a Lebedev scheme in the region of chemical interest were adopted.

The accuracy of the integral calculations was increased to 7, 7, 7, 7 and 14. The self-consistent field (SCF) iterative procedure converged to a tolerance in total energy of $\Delta E = 1 \cdot 10^{-7}$ a.u. The threshold for the maximum and the root-mean- square forces were set to 0.00045 a.u. and 0.0003 a.u.. The Pack-Monkhorst/Gilat shrinking factors for the reciprocal space were set to 6 for the pure CeO_2 and ZnO oxides, and to 5 for the CeO_2/ZnO supercell structure, corresponding respectively to 20, 16 and 15 real reciprocal space points at which the Hamiltonian matrix was diagonalized.

A different fraction α of Hartree-Fock exchange based on dielectric constant value ($\alpha = 1/\varepsilon_\infty$) has been used for CeO_2. α is computed self-consistently without fitting experimental data. This allows to accurately reproduce the band gap (E_g) of pure oxides, necessary precondition for a reliable description of the band alignment [31, 32]. As regards ZnO, the standard HSE06 (α = 25%) already gives a correct E_g value (3.06 eV); for CeO_2 the dielectric-dependent self-consistent procedure gives α = 0.18 with a corresponding E_g = 3.31 eV for the transition from the O 2p band to the Ce 4f states (the computed dielectric constants, 5.4, is in very good agreement with the experimental data, ε_∞ =5.3 [33]).

However, one problem for the description of oxide hetero-junctions is that only one α value can be selected for the composite system. The α value adopted is an average between those that give an accurate description of the two oxides E_g's, i.e. α = 21%. To deal with this problem, we have adopted the same procedure suggested by Pasquarello et al. [34], based on method of the lineup average electrostatic potential at the interface of Van de Walle and Martin [35] and recently used by Conesa [36]. The idea is to take the electrostatic potential inside the solid as a common reference level in order to compare the results of hybrid functional calculations with different α values. The validity of this approach has been evidenced also in the work of Ramprasad et al [37]. This is reasonable considering that the electrostatic potential in a solid is computed with equal accuracy by different functionals. The geometry, the basis set and the pseudopotentials used have to be the same. Finally, the procedure proposes to determine, for each of the pure materials, the positions of the gap edges with respect to the electrostatic potential through calculations that give the correct E_g (by using the mentioned α values). Then the electrostatic potential in the heterostructure model can be computed with any functional, since the electrostatic potential is more or less independent of this choice, and both results are combined to find out the relative band edge positions of the two materials.

3. Results and discussion

3.1 Structural analysis

In Fig. 1 the XRD patterns of undoped ZnO and Ce-doped ZnO (1% mol, CZ1) are reported.

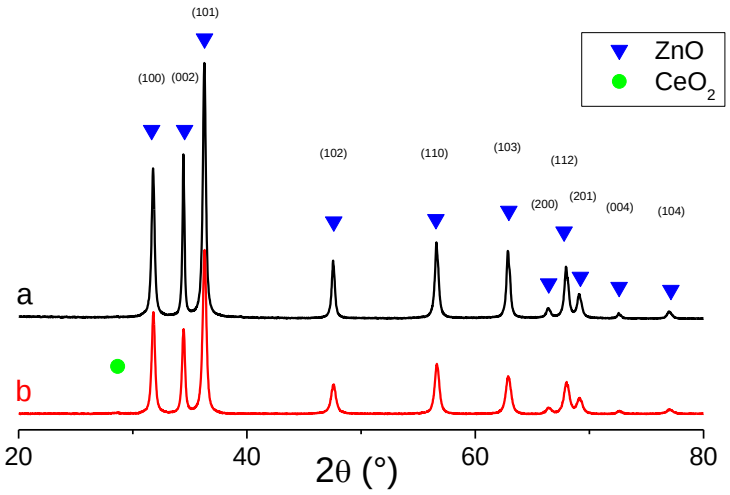

Figure 1 *XRD patterns of the synthetized materials: a) ZnO, b) CZ1. The green dot evidences a weak diffraction peak due to* CeO_2.

Bare ZnO shows the typical pattern of a wurtzite hexagonal phase [38]. No other peak is observed, indicating the high purity of the as-synthetized sample. The diffraction peaks are relatively sharp suggesting the good crystallinity of the final product. The diffractogram of the doped sample, CZ1, is strictly similar to the previous one except for a weak, barely appreciable, peak due to the presence of a CeO_2 phase (green dot in Fig. 1). This peak is much more evident in samples with higher cerium content (data not shown for sake of brevity). The presence of ceria causes a slight broadening of the XRD peaks indicating a smaller crystallites size of the doped sample with respect to the undoped one. This interpretation is confirmed by the Scherrer analysis performed on the XRD patterns, reported in Table 1.

The specific surface areas measured by the BET method are in agreement with Scherrer analysis and, are also listed in table 1; in fact, the doped sample shows the smaller crystallite size and the higher surface area.

Table 1 *Crystallites size, BET surface area and calculated Energy gap for ZnO and CZ1 samples.*

Sample	**d ZnO (nm)**	**d CeO_2 (nm)**	**BET m^2g^{-1}**	**Energy gap**
ZnO	39±3	-	20	3.278
CZ1	27±8	4.3±2	31	3.273

X-ray diffraction data point to a description of the doped material CZ1, in term of a biphasic solid containing small aggregates of CeO_2 rather than a system containing cerium ions dissolved into the ZnO lattice (no alteration of the lattice parameters of ZnO in the mixed sample is detected).

Furthermore, the presence of ceria limits the growth of the ZnO phase, decreasing the crystallite size.

These assumptions were confirmed by TEM analysis in Fig. 2.

For what concerns the bare sample (Fig. 2a and a'), the particles appear with different morphologies. Most of them present platelets shape while a minor fraction shows a rounded profile. The TEM image of the doped sample (Fig. 2b and b') evidences the formation of CeO_2 aggregates of very small size (around 4 nm), mostly with a quasi-spherical shape, stabilized at the surface of ZnO. From a more in-depth analysis, it is noted that the TEM images of the pure ZnO sample (Fig. 2a') show diffraction fringes due to the crystallographic planes (101) and (102). In the case of CZ1 (Fig. 2b'),

the small crystals mostly have diffraction fringes that can be traced back to the crystallographic plane (200) of cerium dioxide.

EDS analysis performed on the doped sample indicates a good dispersion of the Cerium component (data not shown for brevity).

Summarizing, from the structural and morphological analysis of the mixed material (CZ1) it comes out that Ce does not form extrinsic defects entering into the ZnO lattice, as expected considering the different size of Zn^{2+} and Ce^{4+} cations. Rather, electron microscopy and XRD results clearly point to the formation of a colony of small ceria particles anchored to the ZnO surface. This implies the presence in the mixed material of CeO_2-ZnO interfaces or heterojunctions that, as it will be shown in the following, brings about specific photochemical properties of the system. Additionally, the presence of ceria limits the growth of ZnO crystals leading to a material with lower particle size with respect to pristine zinc oxide prepared in the same way.

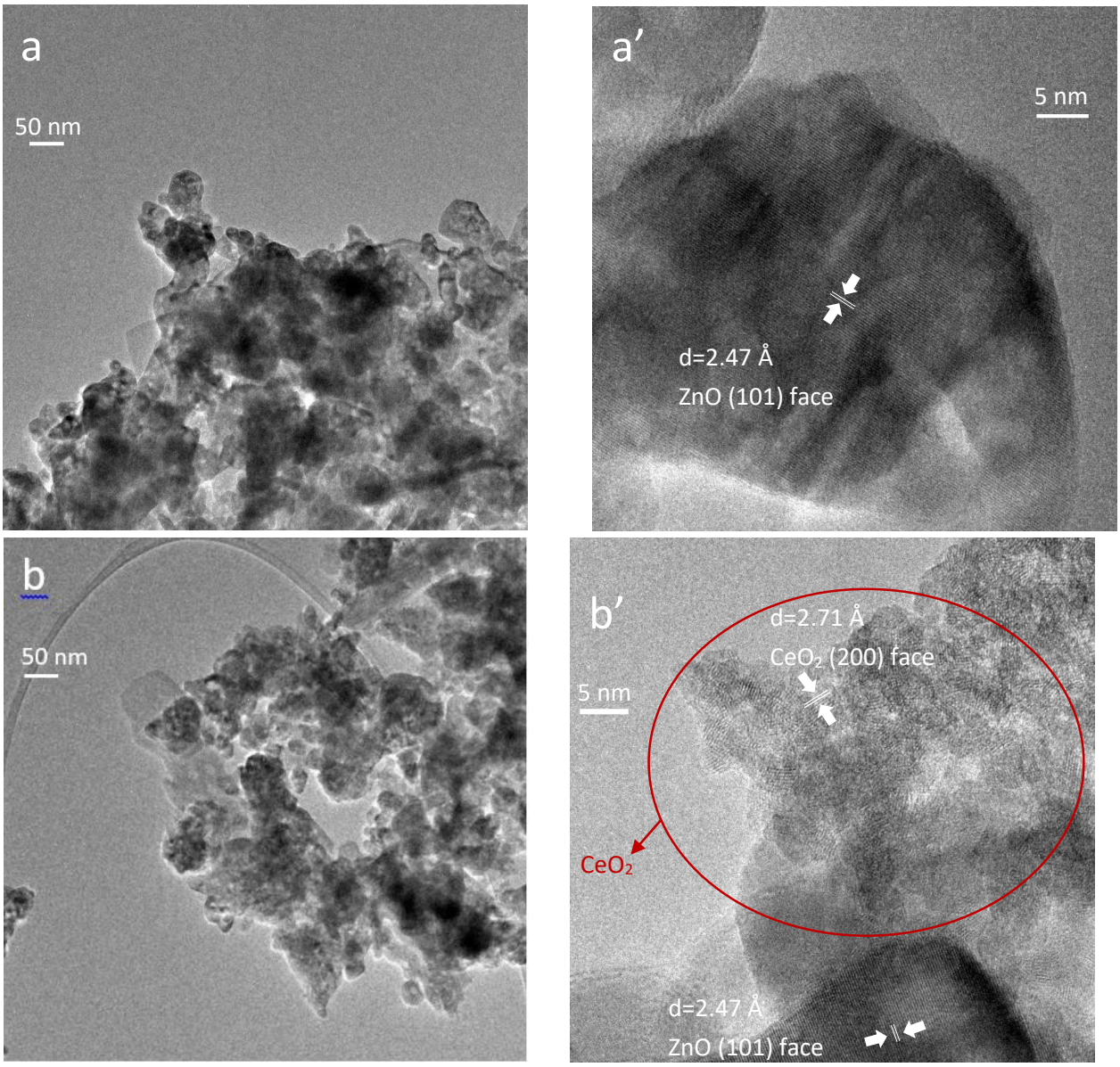

Figure 2 *TEM images of a) ZnO a') ZnO enlargement, b) CZ1 and b') CZ1 enlargement.*

3.2 DRS UV-Vis analysis

In Fig. 3 the UV-Vis diffuse reflectance absorption spectra of both ZnO and CZ1 are reported and compared with the analogous spectrum of bare cerium dioxide. The spectra of both samples are dominated by the valence band (VB) – conduction band (CB) transition of ZnO.

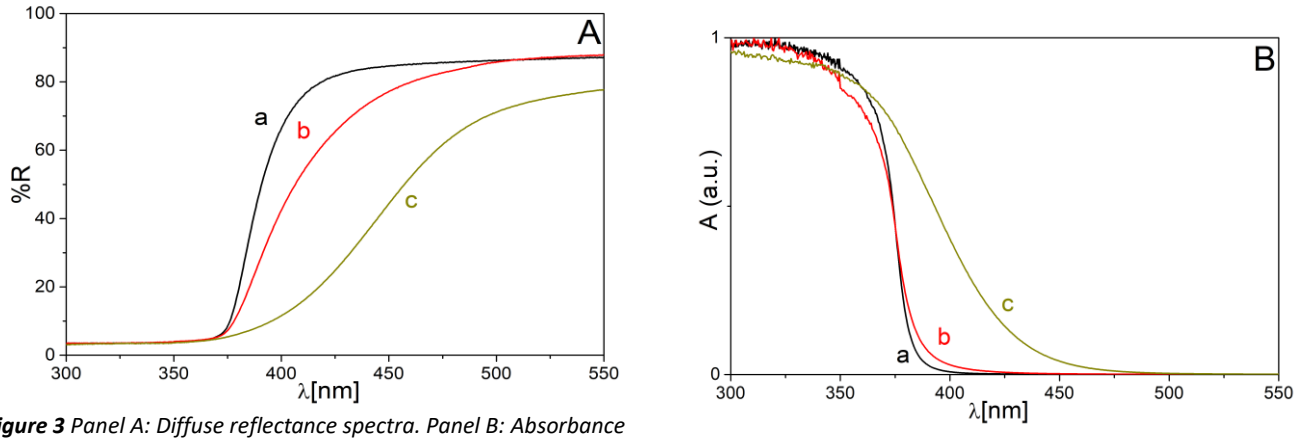

Figure 3 *Panel A: Diffuse reflectance spectra. Panel B: Absorbance Kubelka-Munk transformed diffuse reflectance spectra a) ZnO, b) CZ1, c) CeO_2.*

The presence of a small fraction of ceria in CZ1 slightly modifies the optical properties of ZnO introducing a weak additional absorption around 400 nm with a tail in the visible region. The sample displays a very pale yellow color.

The energy gap of the mixed oxide (Tauc plot, Table 1) is practically unaffected passing from ZnO to CeO_2/ZnO.

3.3 Light induced charge carriers formation and stabilization: EPR evidence

EPR is a suitable technique to monitor the effect of the charge separation processes in semiconducting oxides [39, 40]. Our group recently proposed a series of EPR-based tests to investigate the photoactivity of a given material [12, 41] based on recording EPR spectra under irradiation (or after irradiation) of the material in various conditions. In the simple case of a (diamagnetic) semiconducting oxide irradiated with photons having energy higher than the band gap, the formation of an electron-hole pair occurs with promotion of an electron to the CB and formation of a hole in the VB.

$$MeO_X + h\nu \rightarrow e^-_{(CB)} + h^+_{(VB)} \qquad (1)$$

An electron-hole pair can either recombine or travel in the solid. If the irradiation is performed under vacuum (no surface reaction possible) the electrons surviving recombination are usually stabilized on cations, while the holes are stabilized by oxygen anions.

In the present work, since CeO_2-ZnO materials have shown exciting photocatalytic ability in the abatement of emerging pollutants under solar light irradiation [19], to shed light on the origin of such an activity and on the features of the new system, we have monitored by EPR the charge separation process in CeO_2-ZnO under different conditions of illumination. The same Xe lamp was used in different conditions; a) cut off filter allowing UV irradiation only, without any visible component; b) inserting cut-off filters to select different components of the visible range. This was done for λ>400 nm (a situation similar to the solar irradiation), $\lambda>$ 420 nm (visible light only), and finally at $\lambda>$ 455 nm, $\lambda>$ 495 nm. Irradiation was performed both on samples kept under vacuum (to simply monitor the charge carrier's separation and stabilisation), and, limited to some particular range of frequencies, under either an oxygen or a hydrogen atmosphere to monitor the surface reactivity of the photoexcited carriers. (Section 3.3.2).

In the case of irradiation under vacuum the effects of the charge separation (EPR signals of stabilized e^- and h^+) are observed at 77K. Rising the temperature, fast recombination of the carriers occurs with recovery of the starting EPR spectrum (background). This occurs both for the bare ZnO and for the Ce modified one (CZ1).

3.3.1. Pristine ZnO

The behaviour of pristine ZnO upon illumination in vacuum is described in Fig. 4 (panel A, EPR spectra; panel B quantitative evaluation of the species by double integration of the corresponding EPR signals). The complexity of this matrix, in terms of the unavoidable presence of defects generating intra-band-gap states, is well known and confirmed by the present experiments. For this reason, here we will limit ourselves to analyze the behaviour of the pristine solid in few cases (in order to show the nature of stabilized charge carriers in this solid) devoting a deeper attention to the properties of the mixed CeO_2-ZnO material. The base line of the EPR spectrum of ZnO, recorded in the dark at 77K, is not flat (Fig. 4, panel A, a) showing two distinct signals at g values respectively lower and higher than the free spin value (g_e=2.0023), as previously observed and reported in the literature. The first signal is a quasi-isotropic line at high field (g=1.96) already described by various authors [42-44], whose assignment is still under debate. In fact, it has been attributed to oxygen vacancies [45], shallow donor impurities [46], and interstitial Zn^+ ions. The last assignment, proposed by Halliburton [47], seems the most reasonable, also because signals due to reduced cation species are commonly observed in irradiated reducible oxides [48].

An interpretation about the origin of this EPR signal has been proposed considering interstitial hydrogen atoms acting as electron donor centers [49, 50].

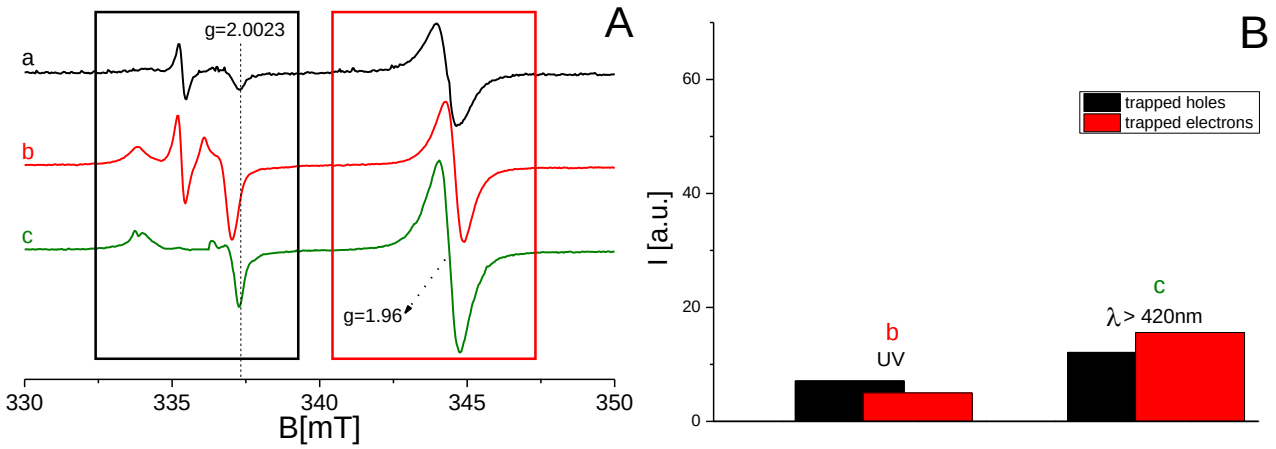

Figure 4 *Panel (A): EPR spectra at 77K of a) activated ZnO, b) after UV-only irradiation, c) after irradiation with λ>420 nm; panel (B) integrated intensities of the EPR signals of trapped electrons and trapped holes as a function of the irradiation wavelength. The intensity of the starting signal in a) (background) has been subtracted from the quantitative values reported in panel B.*

The main features at low field in the background spectrum (Fig. 4A, a) is a weak isotropic line at g=2.014 ubiquitously present in ZnO materials [51] obtained via different procedures and never convincingly assigned.

Irradiation performed selecting two ranges of frequencies (UV-only, and visible-only with λ>420 nm) results in all cases in the growth of the symmetric line at g= 1.96 (Zn^+) indicating the occurrence of electron trapping most probably at cations:

$$e^-_{(CB)} + Zn^{2+} \rightarrow Zn^+ \quad (2)$$

and the parallel appearance of a complex signal at lower field in the region typical of O^- ions [52]. The signal is characterized by $g_\perp$=2.023 and $g_{//}$=2.003 [53-56] and is due to the trapping of photogenerated holes that in a metal oxide occurs according to

$$h^+_{(VB)} + O^{2-} \rightarrow O^- \quad (3)$$

It is somehow surprising that the intensity of the signals of trapped charge carriers is quite similar in the two cases (Fig. 4, panel B). Notice that in the case of UV irradiation nearly all the photons employed have energy higher than the oxide bandgap (3.27 eV - 379 nm) thus allowing the direct excitation from VB to CB. This effect, an apparently paradoxical sensitivity of pristine ZnO to visible light, can only be due to the presence of a rich set of intra-bandgap states in the solid. The complex

interplay of excitation of electrons from and to the intraband states caused by specific photons (already observed in the past in single crystal EPR studies [56, 57]) is the reason of these results and will be discussed in a future paper also on the basis of irradiations with monochromatic light.

A second important observation derived from Fig. 4B is that the ratio between the amount of trapped electron and trapped hole centers in the experiments is around 1 in all cases suggesting that all photo-generated charge carriers are detected by EPR. This is not the case of CeO_2-ZnO materials (*vide infra*). Finally, rising the temperature at 298K after spectra recording, electrons and holes recombine restoring the initial spectrum.

To summarize, the experiment of irradiation on the pristine matrix has revealed the nature and the EPR features of the site trapping the charge carriers in ZnO. These findings will be used for comparison for the case of the mixed Ce-containing material.

3.3.2 CeO_2-ZnO (CZ) materials

The experiments described before (pure ZnO), were repeated using the same amount of the doped sample (CZ1). The spectra obtained upon irradiation of the CZ1 sample are reported in figure 5. The background spectrum (Fig. 5A, a) though weaker, is the same discussed for bare ZnO (Fig. 4a Panel A). The effect of irradiation, in qualitative terms, is also similar as the photogenerated trapped electrons produce a growth both of the g=1.96 signal (Zn^+) and of the signal due to trapped holes, dominated by the axial signal (here at $g_{\perp}$=2.022 and $g_{//}$=2.002) typical of O^- in ZnO. The g tensor parameters of the paramagnetic species observed for CeO_2-ZnO materials are collected in Table 2.

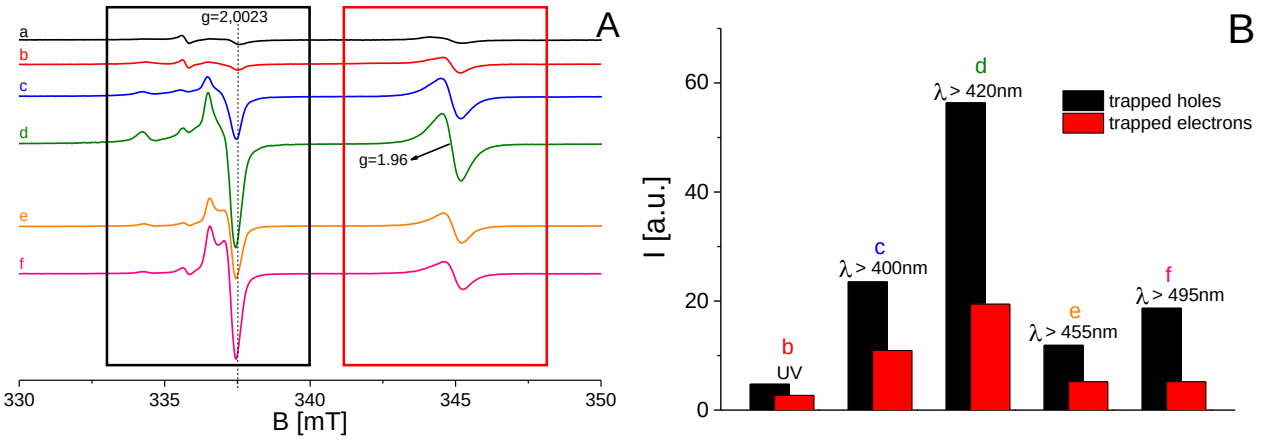

Figure 5 *Panel (A): a) EPR spectra at 77K of activated CZ1 (background in dark), b) after UV-only irradiation, c) after irradiation with λ>400 nm, d) λ>420 nm, e) λ>455 nm; f) 495 nm. Panel (B) integrated intensities of the EPR signals (trapped holes and trapped electrons) as a function of the irradiation wavelength. The intensity of the starting signal in a) (background) has been subtracted from the experimental values.*

The differences in behavior of the two materials (ZnO and CZ1) become evident when the results are compared in quantitative terms (Fig. 5B) as resumed in the following:

a) At variance with the case of ZnO, the amount of trapped holes generated by visible light is systematically higher than that of trapped electrons (Fig. 5, panel B). Since, upon warming the irradiated materials at RT, the initial spectrum is restored by e^- - h^+ recombination, we have to admit that an important fraction of the trapped electrons excited by visible photons is stabilized in some EPR silent form and not as Zn^+ ions. As the same effect is not observed in ZnO (Fig. 4) the presence of ceria must be responsible of this phenomenon. Ce^{3+} ($4f^1$) is a paramagnetic ion, however the high spin orbit constant of cerium prevents the observation of this species by EPR (broad and nearly unappreciable signals even at temperatures much lower than 77K). Our hypothesis, confirmed by theoretical calculations reported below, is therefore that the majority of the photo-excited electrons (those missing in the stick diagram of Fig. 5B) are stabilized by Ce^{4+} ions which reduce to Ce^{3+}. A fraction only of photogenerated electrons is stabilized, in this case, by the ZnO matrix as Zn^+ (g=1.96).

b) The presence of a relatively low amount of Ce (1%) modifies the behaviour of the solid under irradiation in a radical way (Fig 5, panel B). In short, the effects of irradiation with UV light are roughly similar for both bare and Ce modified ZnO materials (Fig 4b and 5b). When the irradiation is instead limited to frequencies in the visible range using different cut-off systems, the photoactivity of cerium modified ZnO (CZ1), in terms of charge separation ability, dramatically increases (Fig. 5 d-f). In particular, the wavelengths around 420 nm are more effective. The highest charge separation (about one order of magnitude higher than that observed using UV–only frequencies) is observed in fact with a cut-off at this particular value (λ> 420nm, Fig. 5 d) i.e. for a range of frequencies roughly corresponding to a purely visible radiation. Selecting irradiations at higher wavelength (λ> 455nm, λ> 495nm, Fig. 5 e-f respectively), the efficiency declines even though it remains higher than in the case of UV illumination. Ce doped ZnO appears therefore as a system with an amazingly prominent visible-light photoactivity.

c) The effect of adding higher energy photons to the visible light range, surprisingly depresses the photoactivity of the system. Just moving the cut-off from 420nm to 400nm reduces of about one half the EPR-monitored photoactivity (5c). High energy photons are therefore detrimental for the charge separation ability of the materials. This counter-intuitive result indicates that the electronic structure of the mixed system is particularly complex, and that

there is a strong interplay between excitation and relaxation processes occurring upon irradiation.

The particular activity in charge separation shown by CeO_2-ZnO upon illumination exclusively with visible light (λ>420 nm) is accompanied by migration of a relevant fraction of the carriers to the surface.

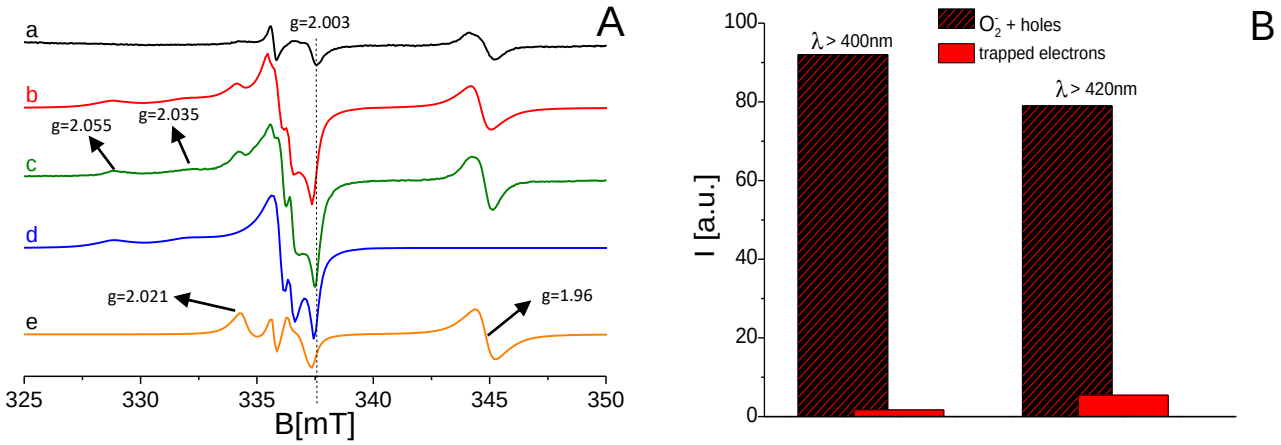

Figure 6 *Panel (A): EPR spectra at 77 K of CZ1 a) background, spectrum in dark, b) irradiation with visible light (λ> 420 nm) in presence of molecular oxygen, c) computer simulation of the whole spectrum b, d) computer simulation limited to the superoxide species (deconvolution of line c), e) computer simulation of all species but superoxide (deconvolution of line c, see text and table 2 below); panel (B) integrated intensities of the EPR spectra upon irradiation in oxygen using UV-only light and λ> 420 nm respectively.*

This is illustrated by the experiment of irradiation in oxygen atmosphere for 15 minutes at λ> 420 nm, reported in Fig. 6 Panel A. It is well known that O_2 acts as an electron scavenger at the surface of an oxide with formation of surface adsorbed O_2^- ions. This reaction testifies the occurrence of migration (and successive reactivity) of photogenerated electrons to the surface

$$e^-_{(CB)} + O_{2\,(gas)} \rightarrow O_2^-{}_{(ads)} \qquad (4)$$

In Figure 6A the EPR spectrum after irradiation in oxygen atmosphere with λ>420 nm is reported (Fig. 6, b) and compared with that of the activated sample (6A, a). The spectrum is dominated by the signals of two distinct species of surface adsorbed superoxide ions indicating the occurrence of the process described in eq. 4. The g tensor of an adsorbed superoxide radical anion has rhombic symmetry with $g_{zz} > g_{yy} > g_{xx} \approx g_e$ and the corresponding signal falls, therefore, in the low field portion of the spectrum (in the same spectral region of trapped holes). The g_{zz} value depends on the electric field exerted on the adsorbed species and is therefore diagnostic of the nature of the adsorbing cation [58]. To better understand the complex nature of the spectrum in Fig. 6A, line b, a computer simulation of the experimental trace has been performed (Fig. 6A, c).

Table 2 *EPR parameters (g values) of the various paramagnetic species observed after irradiation of CeO_2-ZnO (CZ1) with* ʎ > 420 nm

	Nature of the species		g tensor			Note
			g_{zz}	g_{yy}	g_{xx}	
Irradiation under O_2 ʎ > 420 nm	Surface trapped e^-	O_2^- / Zn^{2+}	2.055	2.009	2.003	main species
		O_2^- / Ce^{4+}	$g_\perp$=2.035 $g_{\|\|}$=2.011			
	Bulk trapped e^-	Zn^+	1.960 (isotropic)			
	Trapped h^+	O^-	$g_\perp$=2.022 $g_{\|\|}$=2.003			main species
	Trapped h^+	O^-	$g_\perp$=2.009 $g_{\|\|}$=2.004			
Irradiation under vacuum ʎ > 420 nm	Trapped e^-	Zn^+	1.961 (isotropic)			
	Trapped h^+	O^-	$g_\perp$=2.022 $g_{||}$2.003			main species

The spectrum contains the traces due to two distinct adsorbed superoxide species. The former (g_{zz} = 2.050-2.053 g_{yy}=2.009 and g_{xx}=2.003) is typical of O_2^- adsorbed on Zn^{2+} ions [59-61], while the second one shows the parameters of O_2^- adsorbed on Ce^{4+} ions (g_{zz} = $g_{//}$ =2.032 and g_{yy}= g_{zz} = $g_\perp$=2.011 [62]). Furthermore, the signal at g=1.96 present in the background exhibits a modest growth in intensity after irradiation indicating that a very minor fraction of photoexcited electrons only is stabilized by zinc ions. The portion of the spectrum at g values higher than g_e is actually an envelope produced by the overlap of more than one signal. A satisfactory simulation is obtained only by adding to the two signals of superoxide the contribution of at least another species resonating in this magnetic field range, namely an O^- ions with $g_\perp$=2.022 and $g_{//}$=2.032 (the same observed after irradiation under vacuum).

Figure 6A reports the simulation of the whole spectrum (6c) and, after a partial deconvolution of the simulated trace, the spectral line due to the superoxide species only (on Zn^{2+} and Ce^{4+} respectively, 6d) and that of all the remaining species (Zn^+, O^-, 6e). The high intensity of the integrated spectrum in Fig 6, B, if compared to the intensity shown in Fig. 5 B, is simply due to the overlap in the same spectral region of the signal related to superoxide ions (surface transferred trapped photoelectrons) and trapped holes. In any case, the CZ1 system shows a clear efficiency

under visible light also to transfer electrons toward a scavenger such as O_2. This demonstrates that the photogenerated electrons at λ>420 nm easily reach the surface of the material.

To better understand the complex reactivity observed irradiating the CZ1 sample under oxygen, the reader is referred to the schematic picture reported in the conclusion.

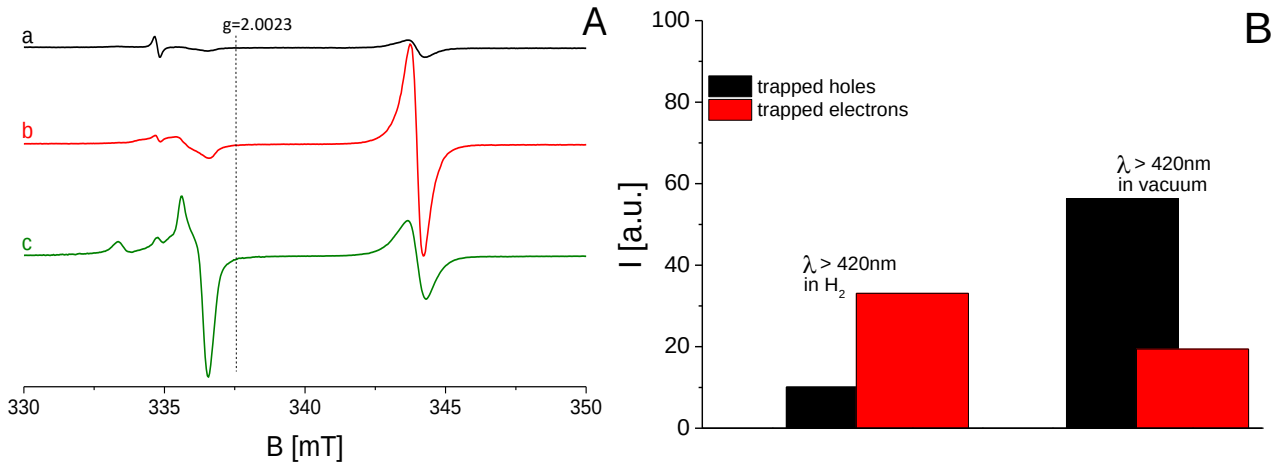

Figure 7 *Panel (A): EPR spectra at 77 K of CZ1 a) background, spectrum in dark, b) after irradiation with visible light (λ>420 nm) in presence of H_2, c) irradiation with λ>420 nm in vacuum.*

The migration of holes to the surface induced by visible light photons is confirmed by a parallel experiment of irradiation in hydrogen atmosphere (Fig. 7, Panel B). It is known that H_2 acts as a hole scavenger, with surface trapped holes generating the homolytic splitting of the H_2 molecule and producing atomic hydrogen:

$$O^-_{(surf)} + H_{2\,(gas)} \rightarrow OH^-_{(surf)} + H^\bullet \qquad (6)$$

The latter is a powerful reducing agent capable of electron injection in the solid [41, 63]. In the case of Fig. 7 b one observes the growth of the EPR signal at g=1.96 indicating that the reduction of Zn^{2+} has occurred.

$$Zn^{2+} + O^{2-}_{(surf)} + H^\bullet_{(gas)} \rightarrow OH^-_{(surf)} + Zn^+ \qquad (7)$$

A parallel reduction of Ce^{4+} ions belonging to the ceria particles is of course also expected, due to the high reducibility of this oxide. This process, however, leads, as before discussed, to EPR undetectable Ce^{3+} ions. The spectra reported in Fig. 7 are less intense than those in Fig. 5. However the comparison of spectra 7b and 7c clearly testify the behaviour of photogenerated holes that

(instead of producing O^- as it occurs by irradiating under vacuum, 7c) reacts with H_2 and eventually determine the formation of trapped electrons only (Zn^+, 7b). However, the peculiar reactivity of the ceria component with the gaseous scavengers makes a quantitative comparison between experiments of irradiation in gaseous atmosphere (Fig. 7) and under vacuum (Fig.5) substantially meaningless. The relevance of the experiments in Fig. 7 is limited to the evidence that, in the mixed material, visible light generates holes, the vast majority of which reach the surface and becomes available for redox interactions.

Summarizing, the mixed material containing ceria particles dispersed at the surface of zinc oxide nanocrystals, shows a particularly attractive photochemical property. The material is based on an oxide (ZnO) with band gap corresponding to the UV range (3.27 eV) of the electromagnetic spectrum, that contains a small amount of surface anchored CeO_2, an oxide with band gap even higher than ZnO. In spite of this fact, the system shows a relevant photoactivity under irradiation with visible light having $\lambda > 420$ nm, here observed in terms of charge separation ability and surface stabilisation of a fraction of the carriers (Fig. 5, 6 and 7) and previously detected in terms of photocatalytic activity [19]. Amazingly, this "full-visible" photoactivity appears to be higher than that observed extending the irradiation to light with λ between 400 nm and 420nm, and higher than that observed using UV light components from 280 nm to 400nm. The whole picture and this latter detail in particular represents, to the best of our knowledge, an unprecedented phenomenon in the field of oxide-based photoactive materials. In the following we address some basic features of the ZnO-CeO_2 hetero-junction based on DFT calculations.

3.4.1. Structure of the hetero-junction

The scope of the calculations is the creation of a model a hetero-junction able to produce a reasonable band alignment of the two oxides, taking into account the complexity of the interface. To build up the composite model, a specific crystallographic face of each pure oxide has to be selected. The choice has to follow specific criteria: (i) small lattice mismatch between the unit cells of the two surfaces; (ii) high stability of the crystallographic faces and; (iii) experimental evidences. Moreover, it is important to highlight that due to computational issues, the net dipole along the non-periodic dimension of the films has to be zero, and that the two-dimensional (2D) film has to be stoichiometric.

In TEM images (Figure 2) the (200) and (101) faces are observed for CeO_2 and ZnO, respectively. However, these two surfaces are not suitable to construct a model of the interface due to (i) a large lattice mismatch, and (ii) the polarity of the (200) CeO_2 surface. Instead, after an accurate analysis, the (111) surface for CeO_2 and the (110) for ZnO have been chosen. Both satisfy all the requirements indicated above. Furthermore, the (111) crystallographic face of CeO_2 is the most stable one and it was reported in previous studies on similar systems [64]. In the case of ZnO, the most stable surface, (001), is polar and thus it cannot be considered. However, the non-polar (110) ZnO surface is reported as quite stable, and already used in a previous theoretical work on a hetero-structure [35].

To reduce the lattice mismatch between the two systems, the (2x2) supercell of the primitive CeO_2 unit cell and the diagonal of the (2x2) ZnO supercell (C(2x2)) have been considered, see Table . The hetero-structure model consists of five CeO_2 layers (about 14 Å thickness) and of ten ZnO layers (16 Å thickness, Figure 2). This size ensures the convergence of the results with respect to the slab thickness, as shown by test calculations on thicker slabs.

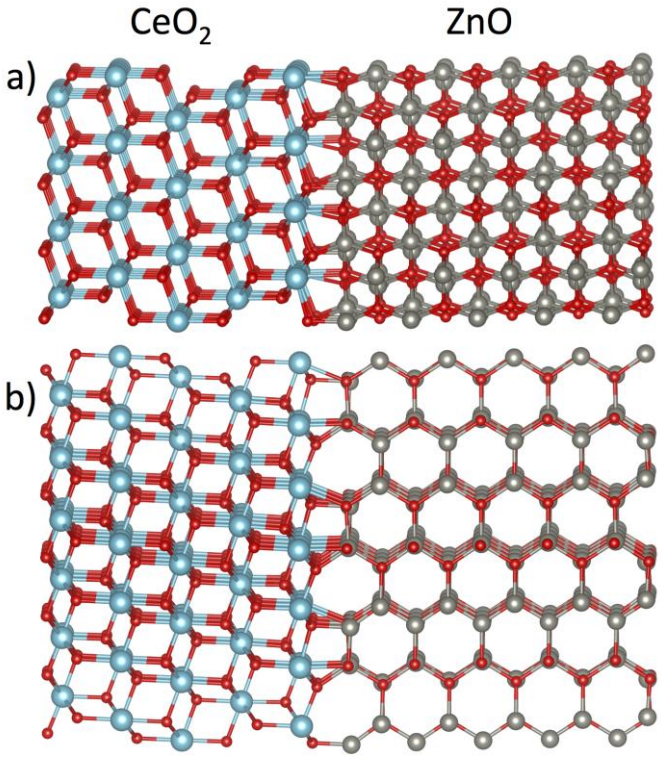

***Figure 8**: Side views of the relaxed hetero-junction (a, b). Light blue spheres represent Ce atoms, grey Zn, and red O.*

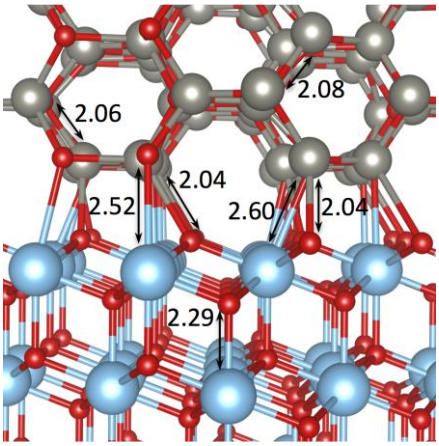

***Figure 9**: Magnification of the relaxed hetero-structure at the interface. Main bond lengths are reported in Å. Light blue spheres represent Ce atoms, grey Zn and red O.*

In Table 3 the optimized cell parameters are reported accompanied by band gap energies of the two bare, separated oxides (slab calculations). The lattice mismatch of the two oxides is very small for a and b, i.e. 1.6%; on the contrary, the difference on γ is relevant, 27% (120° and 94° for CeO_2 and ZnO, respectively). The strain can be equally distributed on both systems; the starting junction 2D cell parameters are characterized by averaged values of the two oxide cells. This leads to a lattice mismatch of 0.8% for a and b and of 13.6% for γ.

***Table 3**: Cell parameters (Å and degrees), percentage differences (Δ%) and band gap of the ZnO and CeO_2 surfaces. Δ% of relaxed ZnO/CeO_2 are computed with respect to CeO_2 (111). HSE results.*

Surfaces	supercell	a (Å)	Δ%	b (Å)	Δ%	γ	Δ%	E_g
(110) ZnO	C(2x2)	7.704		7.704		94.4		3.15
(111) CeO_2	(2x2)	7.582	1.6	7.581	1.6	120	27.1	3.14
ZnO/CeO_2		7.530	0.7	7.531	0.7	114.4	4.7	

In Figure 8, the fully relaxed hetero-junction structure is reported (both atomic coordinates and cell parameters have been optimized). During the optimization, the cell of the hetero-structure tends to reduce its volume, and becomes “more” hexagonal. The result is a cell with parameters very close to those of CeO_2 (the strain, Δ, is smaller than 1%); the final γ value is 114°, and the difference with respect to the CeO_2 angle is reduced by almost 10% (from 14% to less than 5%, Table)). The structure of CeO_2 appears to be more rigid than that of wurtzite ZnO that, on the contrary, is easily deformed. ZnO tends to adapt its structure to the hexagonal cell of the (111) CeO_2 surface. This can be related to the existence of numerous polymorphs of ZnO.

An interesting atomic arrangement is observed at the interface; new - -Ce—O- - and - -Zn—O- - bonds are formed following in part the structure of wurtzite, in part that of CeO_2 (see bond lengths

in Figure). The position of the atoms lying in the central slabs of the two oxides is representative of those in the bulk, as expected.

3.4.2. Electronic Structure and Band Alignment

The band positions of the two oxides have been estimated by the line-up averaged electrostatic potential (V) method [34, 35]. The first step is the calculation of the electrostatic potential V in the relaxed hetero-junction model using the hybrid functional with α = 0.21, an average value for the two oxides. This is computed by using a grid of 0.125 Å and the potential is averaged in each atomic plane parallel to the surface, see Figure 0a. The plot is reported with respect to the non-periodic axis (Z) normal to the interface plane; the sharp minima correspond to the planes of the atomic positions. In Figure 0b, the two parts corresponding to CeO_2 and ZnO are shown; V in the inner zone of the two oxides remains more or less at the same energy, while it changes in correspondence of the oxide/oxide and oxide/vacuum interfaces due to both geometrical distortions and electronic effects (including charge transfer at the interface). To align the levels we follow the procedure suggested by Conesa [36]. The reference value is taken as the point where the derivative of V is zero (E_{top}, see Figure 0a). This value changes slightly close to the interface; therefore, we selected one of the maxima in the central region of the oxides film, better representing the bulk of the oxide. For the hetero-junction, E_{top} correspond to -2.61 eV for CeO_2 and -4.36 eV for ZnO, Figure 10.

The second step involves the calculation of the same quantity, E_{top}, for the pure, isolated CeO_2 and ZnO phases using an optimal hybrid functional where the α values were obtained for the undistorted cells (dielectric-dependent and material-dependent α) and without any further relaxation. The pure oxides are thus computed at the distorted geometry of the hetero-structure; in this way the geometrical effect of lattice distortion is considered. We refer to these systems as CeO_2[Het] and ZnO[Het]. In this way we obtained E_{top} as well as the E_g values for the distorted structures, E_g = 3.07 eV for CeO_2 and E_g = 3.11 eV for ZnO, respectively, Figure 10. In both cases, the two values are very close to those computed for the corresponding free, undistorted slabs 3.14 eV for CeO_2(111) and 3.15 eV for ZnO (110), see Table 3.

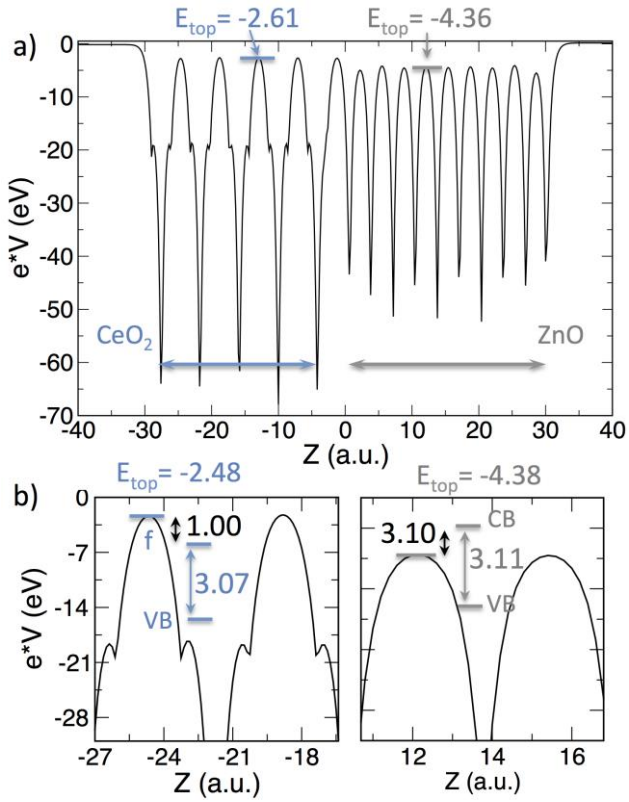

***Figure 10**: Electrostatic potential (V*e) of a) the hetero-junction and of b) CeO_2[Het] and ZnO[Het] averaged in a plane parallel to the surface with respect to the non-periodic Z coordinate. E_{top} for the two oxide components have been reported (eV). The alignment of the band edges with respect to E_{top} and the energy gap in the separated CeO_2[Het] and ZnO[Het] systems are also shown (in eV).*

The electrostatic potential obtained for the real hetero-structure and for the separated CeO_2[Het] and ZnO[Het] units obtained following the procedure described above are shown in Figure 0. The VB and CB positions, as obtained from the Kohn-Sham orbital energies, are aligned with respect the reference level (E_{top}) for the two structurally deformed oxides (CeO_2[Het] and ZnO[Het]). We can now transfer the energy difference between the CB's and E_{top} to the reference level obtained for the real relaxed hetero-junction, and obtain the scheme of band alignment of the two oxides, see Figure 1a. In this diagram, the VB of ZnO lies 0.45 eV above that of CeO_2; at the same time, the ZnO CB is about 0.40 eV higher than Ce 4f states, see Figure 1a. Notice however that this scheme is not final as it is affected by the large strain present in the hetero-junction. We will see in the next paragraph how to correct for this effect.

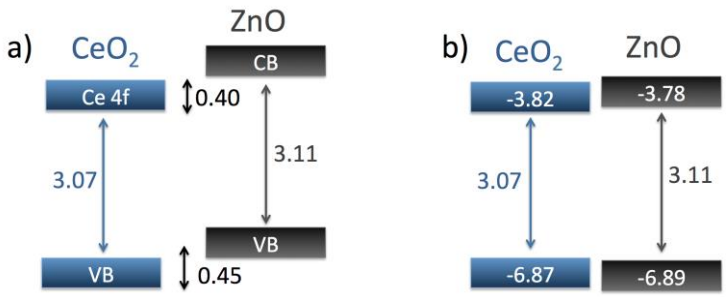

***Figure 11**: Schematic diagram of the ZnO/CeO_2 band alignment for the composite system (a) including the strain resent in the hetero-junction and (b) after the strain correction. Values are reported in eV.*

As we mentioned above, the large distortion of the lattice parameter γ in our model of the hetero-junction can affect the band positions. In principle, the problem could be overcome by considering very large supercells, such as to minimize the strain due to the mismatch between the two oxide structures. The need to keep computational costs at a reasonable level forces us to use a moderate size cell of 168 atoms where some residual strain is present. In the following we discuss a procedure to take into account the strain and correct the results reported in Figure 11a by this effect.

First, we computed the band edges of the two pure oxide structures in the same optimal cell of the relaxed hetero-junction, and we relax only the internal coordinates (atomic positions). This allows us to estimate the contribution of the atomic rearrangement due to the lattice mismatch on the band positions. Indeed, a rigid up shift of +0.21 eV for CeO_2 and of +0.68 eV for ZnO of both VBs and CBs has been obtained in these calculations. Starting from the consideration that this shift is only a consequence of the internal strain due to the small supercell, we have subtracted these contributions from the band positions computed for the CeO_2[Het] and ZnO[Het] slabs, Figure 11a. This leads the final estimate of the band alignment in the hetero-structure, which is shown in Figure 11b. Here the VBs of the two oxide semiconductors lie almost at the same energy; furthermore, since the two band gaps are also similar, also the CBs are nearly degenerate.

Of course, this discussion shows that (a) the lattice mismatch plays an important role in the band alignment of the junction; and (b) a number of approximations need be done before to arrive at the final result, which therefore has to be taken with some care.

Having established the band alignment of the two oxides in the hetero-junction, we can now proceed and analyse the nature and energy associated to electronic excitations in this system.

3.4.2 Electronic excitations

In this Section we consider the process occurring when the CeO_2/ZnO hetero-junction in its ground state is perturbed by the interaction with UV-vis light. To this end, we first consider the nature of the lowest excited state obtained starting from the unperturbed system. To this end we computed the total energy of the triplet excited configuration, which can be considered as a reasonable approximation of the lowest excited state of the real system. In order to create a triplet configuration, one electron has to be promoted from the top of the VB to the lowest available electronic states. In this calculation no approximation is made, and the result will reflect the most stable solution when electrons are promoted from the VB to the CB. The nature of the triplet excited state is well described by a spin density plot, Figure 2.

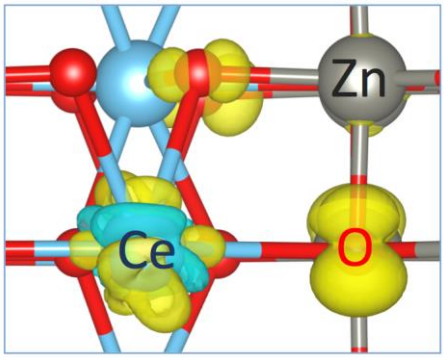

***Figure 12**: Spin density plot of relaxed CeO_2/ZnO triplet state (isodensity threshold values 0.007 e/a.u.^{3}).*

The excited state is characterized by the presence of two unpaired electrons, one fully localized on a 4f orbital of an interface Ce ion, and one partly delocalized over O atoms, two from ZnO and two from the CeO_2 units. The triplet configuration is 1.9 eV higher than the singlet ground state. This result is very important since it shows that the lowest excitation in the hetero-junction involves the promotion of one electron from the O 2p valence band to a Ce 4f orbital, with consequent reduction of Ce^{4+} to Ce^{3+} at the interface. While the excited electron is thus fully localized, the resulting hole (h^+) is shared among some O atoms of the two oxides at the interface. This is exactly what is expected based on the approximated energy diagram of Figure b: the top of the VBs of the two oxides are almost at the same energy, hence it is not surprising that the photo-generated hole is shared between the two oxides, indicating high mobility of this species, while the photo-generated electron is trapped at a specific Ce ion.

The next step is to try to evaluate more quantitatively the energy involved in the photo-excitation. The diagram of Figure 11 is based on the Kohn-Sham energy levels and cannot provide this

information. For the interpretation of the experimental results, the calculation of the energies involved in electronic transitions has to be performed. It is common practice to estimate the semiconductor band gap and the energy levels introduced in the gap by defects by considering the transition energy levels (CTLs) approach where total energies of different electronic states are considered instead of one-electron Kohn-Sham energies. In the CTL calculations energy differences between different charge states for a defective system are considered. The transition level ε[(q + 1)/q] is defined as the Fermi level, referred to the top of the VB, for which the formation energies of defects in the charge states q + 1 and q are equal. The CTLs can be derived on the basis of Janak's theorem [65].

This method is rather accurate when used in connection with hybrid functionals that provide a good estimate of the Kohn–Sham band gap of the system. In particular, optical transition levels (ε_{opt}) can be directly compared with the position of the defect levels estimated from optical excitation [65, 66].

As we have seen above, the important transition here is the Ce^{4+} reduction at the interface: $Ce^{4+} + 1e^{-} \rightarrow Ce^{3+}$. The calculation of CTL for this process has been performed by adding one electron to the composite system. It shows that the transition from the VB to a Ce^{4+} cation, leading to Ce^{3+}, occurs at 2.3 eV, that is well inside of the visible light spectrum (see Figure). Notice that this optical transition energy is of comparable magnitude of the singlet-triplet excitation discussed above (1.9 eV).

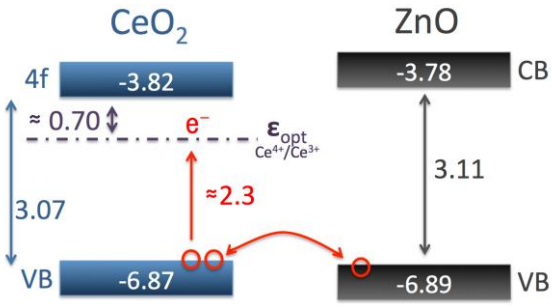

***Figure 13**: Schematic diagram of the final ZnO/CeO_2 band alignment and possible photoexcitation of the composite system. Values are reported in eV.*

This confirms the experimental evidences reported in Subsection 3.3.2., which suggests that an important fraction of the photo-excited electrons (by visible light) is stabilized by Ce^{4+} ions that are thus reduced to Ce^{3+} (invisible in EPR for reasons discussed above). This value is also in very good agreement with previous data obtained for Ce-doped ZrO_2 [67] where the Ce ions are diluted into

the ZrO_2 matrix. In Figure 14 a simplified diagram is presented where the excitation occurring at the CeO_2/ZnO interface is reported in addition to other processes occurring in the bulk of ZnO.

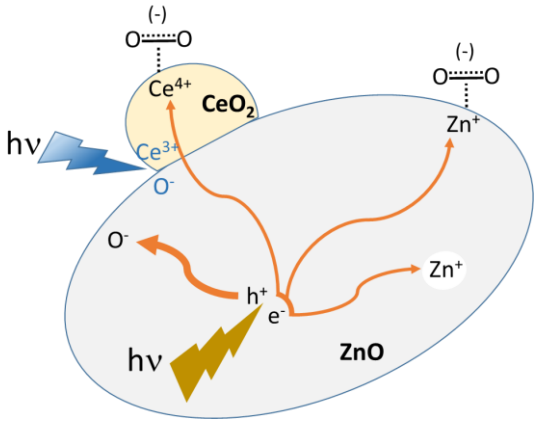

Figure 14: *Schematic representation of the chemistry observed upon irradiation of CeO_2/ZnO under oxygen atmosphere.*

4. Conclusions

The formation of hetero-junctions between CeO_2 and ZnO has been observed experimentally (Electron microscopy and XRD) and simulated by DFT calculations (hybrid DFT functionals). The presence in the mixed material of CeO_2/ZnO interfaces appears responsible of specific photochemical properties. The material is composed by segregated CeO_2 nanoparticles supported on larger ZnO nanostructures.

The mixed-material is based on two oxides with band gap values corresponding to UV range (≈3.3 eV). As shown by a UV-vis analysis, this band gap is not affected by the formation of the hetero-junction.

Nevertheless, the presence of relatively low amounts of Ce (1%) the behaviour of the solid under irradiation changes in a radical way. The irradiation with frequencies in the visible range notably increases the photoactivity of the CeO_2/ZnO system both in terms of number of charge carrier available and of charge separation ability, as illustrated by EPR spectroscopy. The experiments of irradiation in oxygen and hydrogen atmosphere showed that a relevant fraction of the photogenerated charge carriers are able to migrate and react at the surface.

Moreover, an important amount of the trapped electrons excited by photons with energy in the visible range is stabilized in some EPR silent form, but not as Zn^+ ions. Most likely, the majority of the photo-excited electrons are stabilized by Ce^{4+} ions, which in turn are reduced to Ce^{3+}, not visible in EPR spectra.

These experimental evidences are in agreement with the computed band alignment of the two oxides in the hetero-junction. A theoretical model composed by the junction of the (111) CeO_2 and the (110) ZnO surfaces has been built and fully optimized. The lineup averaged electrostatic potential approach has been adopted to represent the band alignment of the composite model. It turns out that the valence bands of the two oxides lie almost at the same energy, and, considering the similar E_g, also the conduction band of ZnO and the Ce 4f states of CeO_2 are nearly degenerate. This may result in a higher mobility of the photo-generated holes on the two systems, thus retarding the e^--h^+ recombination. Moreover, by computing the charge transition levels, we are able to conclude that the process $O^{2-} + Ce^{4+} \rightarrow O^- + Ce^{3+}$ has a transition energy that lies in the visible range (2.3 eV) and that the excitation involves species near the interface. Of course, further complexity in the model is associated to the presence of defects at the interface and in the bulk of the two materials, an effect that has not been considered in the present models. Nevertheless, we believe that the model captures some of the key features of the CeO_2/ZnO interface.

However, an unclear phenomenom also occurs; from EPR results it is clear that the wavelengths around 420 nm are the most effective for the photoactivity. Higher energy photons surprisingly depress the photoactivity of the system; apparently, they have a detrimental effect on the charge separation. This result indicates that the electronic structure of the mixed system is particularly complex. A possible explanation can be related to the recombination tendency in ZnO. Uv light is indeed able to excite electrons directly to the ZnO CB and it appears that the recombination between electrons in the ZnO CB and holes in the VB is quite fast and immediately suppresses the photoactivation. On the contrary, lower energy photons lead to the excitation of electrons from the ZnO VB to the Ce states, a process that retards the recombination.

Mixing Ce and ZnO produces a system with an amazingly prominent visible-light photoactivity. Some observed features still need to be convincingly explained and are attributed to the complexity of the system, and in particular of the ZnO phase. Further work is required in order to fully understand the nature of this interesting material.

Acknowledgment

Financial support from the Italian MIUR through the PRIN Project 2015K7FZLH, SMARTNESS “Solar driven chemistry: new materials for photo- and electro-catalysis” is gratefully acknowledged.

References

[1] C. Figures, H.J. Schellnhuber, G. Whiteman, J. Rockström, A. Hobley, S. Rahmstorf, Three years to safeguard our climate, Nature 546 (2017) 593-595.
[2] Y. Xu, V. Ramanathan, Well below 2 degrees C: Mitigation strategies for avoiding dangerous to catastrophic climate changes, Proc. Natl. Acad. Sci. U. S. A., 114 (2017) 10315-10323.
[3] Y. Tachibana, L. Vayssieres, J.R. Durrant, Artificial photosynthesis for solar water-splitting, Nature Photonics, 6 (2012) 511-518.
[4] K. Hashimoto, H. Irie, A. Fujishima, TiO2Photocatalysis: A Historical Overview and Future Prospects, Jpn. J. Appl. Phys., 44 (2005) 8269-8285.
[5] D. Ravelli, S. Protti, A. Albini, Energy and molecules from photochemical/photocatalytic reactions. An overview, Molecules, 20 (2015) 1527-1542.
[6] D. Ravelli, D. Dondi, M. Fagnoni, A. Albini, Photocatalysis. A multi-faceted concept for green chemistry, Chem. Soc. Rev., 38 (2009) 1999-2011.
[7] A. Fujishima, K. Honda, Electrochemical Photolysis of Water at a Semiconductor Electrode, Nat. Biotechnol., 238 (1972) 37-38.
[8] T. Hisatomi, J. Kubota, K. Domen, Recent advances in semiconductors for photocatalytic and photoelectrochemical water splitting, Chem. Soc. Rev., 43 (2014) 7520-7535.
[9] K. Takanabe, K. Domen, Preparation of Inorganic Photocatalytic Materials for Overall Water Splitting, Chem. Cat. Chem., 4 (2012) 1485-1497.
[10] M. Kodera, J. Wang, B.A. Nail, J. Liu, H. Urabe, T. Hisatomi, M. Katayama, T. Minegishi, F.E. Osterloh, K. Domen, Investigation of charge separation in particulate oxysulfide and oxynitride photoelectrodes by surface photovoltage spectroscopy, Chem. Phys. Lett., 683 (2017) 140-144.
[11] R. Asahi, T. Morikawa, T. Ohwaki, K. Aoki, Y. Taga, Visible-Light Photocatalysis in Nitrogen-Doped Titanium Oxides, Science, 293 (2001) 269-271.
[12] C. Gionco, M.C. Paganini, E. Giamello, R. Burgess, C. Di Valentin, G. Pacchioni, Cerium-Doped Zirconium Dioxide, a Visible-Light-Sensitive Photoactive Material of Third Generation, J. Phys. Chem. Lett., 5 (2014) 447-451.
[13] O. Bechambi, A. Touati, S. Sayadi, W. Najjar, Effect of cerium doping on the textural, structural and optical properties of zinc oxide: Role of cerium and hydrogen peroxide to enhance the photocatalytic degradation of endocrine disrupting compounds, Mater. Sci. Semicond. Process., 39 (2015) 807-816.
[14] C. Jayachandraiah, G. Krishnaiah, Influence of cerium dopant on magnetic and dielectric properties of ZnO nanoparticles, Journal of Materials Science, 52 (2017) 7058-7066.
[15] C. Gionco, M.C. Paganini, E. Giamello, O. Sacco, V. Vaiano, D. Sannino, Rare earth oxides in zirconium dioxide: How to turn a wide band gap metal oxide into a visible light active photocatalyst, J. Energy Chem., 26 (2017) 270-276.
[16] M. Chiesa, E. Giamello, M. Che, EPR Characterization and Reactivity of Surface-Localized Inorganic Radicals and Radical Ions, Chem. Rev., 110 (2010) 1320-1347.
[17] E.G. Panarelli, S. Livraghi, S. Maurelli, V. Polliotto, M. Chiesa, E. Giamello, Role of surface water molecules in stabilizing trapped hole centres in titanium dioxide (anatase) as monitored by electron paramagnetic resonance, J. Photochem. Photobiol., A, 322-323 (2016) 27-34.
[18] C. Gionco, M.C. Paganini, M. Chiesa, S. Maurelli, S. Livraghi, E. Giamello, Cerium doped zirconium dioxide as a potential new photocatalytic material. The role of the preparation method on the properties of the material, Applied Catalysis A: General, 504 (2015) 338-343.
[19] P. Calza, C. Gionco, M. Giletta, M. Kalaboka, V.A. Sakkas, T. Albanis, M.C. Paganini, Assessment of the abatement of acelsulfame K using cerium doped ZnO as photocatalyst, J. Hazard. Mater., 323 (2016) 471-477.
[20] S. Livraghi, M.C. Paganini, E. Giamello, A. Selloni, C.D. Valentin, G. Pacchioni, Origin of Photoactivity of Nitrogen-Doped Titanium Dioxide under Visible Light, J. Am. Chem. Soc., 128 (2006).

[21] G. Barolo, S. Livraghi, M. Chiesa, M.C. Paganini, E. Giamello, Mechanism of the Photoactivity under Visible Light of N-Doped Titanium Dioxide. Charge Carriers Migration in Irradiated N-TiO2 Investigated by Electron Paramagnetic Resonance, J. Phys. Chem. C, 116 (2012) 20887-20894.
[22] X. Wang, L. Huang, Y. Zhao, Y. Zhang, G. Zhou, Synthesis of Mesoporous ZnO Nanosheets via Facile Solvothermal Method as the Anode Materials for Lithium-ion Batteries, Nanoscale Res. Lett., 11 (2016) 37.
[23] A. Adamski, T. Spalek, Z. Sojka, Application of EPR spectroscopy for elucidation of vanadium speciation in VO_x/ZrO_2 catalysts subject to redox treatment, Res. Chem. Intermed., 29 (2003) 793-804.
[24] A.V. Krukau, O.A. Vydrov, A.F. Izmaylov, G.E. Scuseria, Influence of the exchange screening parameter on the performance of screened hybrid functionals, J. Chem. Phys., 125 (2006) 224106.
[25] J. Heyd, G.E. Scuseria, M. Ernzerhof, Hybrid functionals based on a screened Coulomb potential, The Journal of Chemical Physics, 118 (2003) 8207-8215.
[26] J. Heyd, G.E. Scuseria, Assessment and validation of a screened Coulomb hybrid density functional, J. Chem. Phys., 120 (2004) 7274-7280.
[27] R. Dovesi, R. Orlando, A. Erba, C.M. Zicovich-Wilson, B. Civalleri, S. Casassa, L. Maschio, M. Ferrabone, M. De La Pierre, P. D'Arco, Y. Noël, M. Causà, M. Rérat, B. Kirtman, CRYSTAL14: A program for theab initioinvestigation of crystalline solids, Int. J. Quantum Chem, 114 (2014) 1287-1317.
[28] Y. Hinuma, A. Grüneis, G. Kresse, F. Oba, Band alignment of semiconductors from density-functional theory and many-body perturbation theory, Physical Review B, 90 (2014) 155405.
[29] M. Dolg, H. Stoll, H. Preuss, Energy-adjustedabinitiopseudopotentials for the rare earth elements, The Journal of Chemical Physics, 90 (1989) 1730-1734.
[30] J. Graciani, A.M. Màrquez, J.J. Plata, Y. Ortega, N.C. Hernàndez, A. Meyer, C.M. Zicovhic-Wilson, J. Fdez, Comparative Study on the Performance of Hybrid DFT Functionals in Highly Correlated Oxides: The Case of CeO_2 and Ce_2O_3, J. Chem. Theory Comput., 7 (2011) 56-65.
[31] J.H. Skone, M. Govoni, G. Galli, Self-consistent hybrid functional for condensed systems, Physical Review B, 89 (2014) 195112.
[32] M. Gerosa, C.E. Bottani, L. Caramella, G. Onida, C. Di Valentin, G. Pacchioni, Defect calculations in semiconductors through a dielectric-dependent hybrid DFT functional: The case of oxygen vacancies in metal oxides, J. Chem. Phys., 143 (2015) 134702.
[33] A. Calzolari, M.B. Nardelli, Dielectric properties and Raman spectra of ZnO from a first principles finite-differences/finite-fields approach, Scientific reports, 3 (2013) 2999.
[34] A. Alkauskas, P. Broqvist, A. Pasquarello, Defect levels through hybrid density functionals: Insights and applications, physica status solidi (b), 248 (2011) 775-789.
[35] C.G. Van de Walle, R.M. Martin, Theoretical study of band offsets at semiconductor interfaces, Physical Review B, 35 (1987) 8154-8165.
[36] J.C. Conesa, Modeling with Hybrid Density Functional Theory the Electronic Band Alignment at the Zinc Oxide–Anatase Interface, The Journal of Physical Chemistry C, 116 (2012) 18884-18890.
[37] R. Ramprasad, H. Zhu, P. Rinke, M. Scheffler, New perspective on formation energies and energy levels of point defects in nonmetals, Phys. Rev. Lett., 108 (2012) 066404.
[38] O. Bechambi, L. Jlaiel, W. Najjar, S. Sayadi, Photocatalytic degradation of bisphenol A in the presence of CeeZnO: Evolution of kinetics, toxicity and photodegradation mechanism, Mater. Chem. Phys., 173 (2016) 95-105.
[39] R.F. Howe, M. Gratzel, Electron-Paramagnetic-Res Study of Hydrated Anatase Under UV Irradiation, J. Phys. Chem., 91 (1987) 3906-3909.
[40] O.I. Micic, Y.N. Zhang, K.R. Cromack, A.D. Trifunac, M.C. Thurnauer, Photoinduced hole transfer from TIO_2 to methanol molecules in acqueous-solution studied by Electron-Paramagnetic-Resonance, J. Phys. Chem., 97 (1993).
[41] M. Chiesa, M.C. Paganini, S. Livraghi, E. Giamello, Charge trapping in TiO2 polymorphs as seen by Electron Paramagnetic Resonance spectroscopy, Phys. Chem. Chem. Phys., 15 (2013) 9435-9447.
[42] P.H. Kasai, Electron Spin Resonance Studies of Donors and Acceptors in ZnO, Phys. Rev., 130 (1963) 989-995.
[43] C. Klingshirn, J. Fallert, H. Zhou, J. Sartor, C. Thiele, F. Maier-Flaig, D. Schneider, H. Kalt, 65 years of ZnO research - old and very recent results, Phys. Status Solidi B, 247 (2010) 1424-1447.

[44] F. Morazzoni, R. Scotti, S. Volontè, Electron Paramagnetic Resonance Investigation of Paramagnetic Point Defects in ZnO and ZnO-supported Ruthenium, J. Chem. Soc. Faraday Trans., (1990) 1587-1591.
[45] R.B. Lal, G.M. Arnett, Electron Paramagnetic Resonance of Photosensitive Donors in ZnO, J. Phys. Soc. Jpn., 21 (1966) 2734-2735.
[46] D.M. Hofmann, A. Hofstaetter, F. Leiter, H. Zhou, F. Henecker, B.K. Meyer, S.B. Orlinskii, J. Schmidt, P.G. Baranov, Hydrogen: a relevant shallow donor in zinc oxide, Phys. Rev. Lett., 88 (2002) 045504.
[47] L.E. Halliburton, N.C. Giles, N.Y. Garces, M. Luo, C. Xu, L.B.A. Boatner, Production of native donors in ZnO by annealing at high temperature Zn vapour, Appl. Phys. Lett., 87 (2005).
[48] R.D. Iyengar, TiO_2 and ZnO Surface Studies by Electron Spin Resonance Spectroscopy, Advan. Colloid Interface Sci., 3 (1972) 365-388.
[49] C.G.V.d. Walle, Hydrogen as a Cause of Doping in Zinc Oxide, Phys. Rev. Lett., 85 (2000) 1012-1015.
[50] K. Hoffmann, D. Hahn, Electron Spin Resonance of Lattice Defects in Zinc Oxide, phys. stat. sol. (a), 24 (1974) 637-648.
[51] J.H. Lunsford, J.P. Jayne, Electron Paramagnetic Resonance of Oxygen on ZnO and UltravioletIrradiated MgO J. Chem. Phys., 44 (1966) 1487-1492.
[52] C.D. Valentin, D. Ricci, G. Pacchioni, M. Chiesa, M.C. Paganini, E. Giamello, O- radical anions on polycrystalline MgO, Surf. Sci., 521 (2002).
[53] N.B. Wong, Y.B. Taarit, J.H. Lunsford, Formation of O− in ZnO from the dissociation of adsorbed N_2O, J. Chem. Phys., 60 (1974) 2148-2151.
[54] A.M. Volodin, A.E. Cherkashin, ESR Studies of N_2O interaction with photoinduced centers on ZnO and MgO React. Kinet. Catal. Lett., 20 (1982) 335-338.
[55] A.M. Volodin, S.E. Malykhin, G.M. Zhidomirov, O− radical anions on oxide catalysts: Formation, properties, and reactions, Kinet. Catal., 52 (2011) 605-619.
[56] K. Leutwein, J. Schneider, Defects in Neutron-irradiated ZnO, Z. Naturforsch., 26a (1971) 1236-1237.
[57] D. Gallad, A. Herve, ESR Spectro of the Zinc Vacancy in ZnO, Phys. Lett., 33 (1970) 1-2.
[58] M. Chiesa, E. Giamello, M.C. Paganini, Z. Sojka, D.M. Murphy, Continuous wave electron paramagnetic resonance investigation of the hyperfine structure of 17O2− adsorbed on the MgO surface, J. Chem. Phys., 116 (2002) 4266-4274.
[59] R.D. Iyengar, V.V.S. Rao, A.C. Zettlemoyer, ESR Studies of the Interaction of O_2, NO_2, N_2O, NO and Cl_2 with Zinc Oxide, Surf. Sci., 13 (1969) 251-262.
[60] R. Lindsay, E. Michelangeli, B.G. Daniels, M. Polcik, A. Verdini, L. Floreano, A. Morgante, J. Muscat, N.M. Harrison, G. Thornton, Surface to bulk charge transfer at an alkali metal/metal oxide interface, Surf. Sci., 547 (2003) L859-L864.
[61] M. Iwamoto, Y. Yoda, N. Yamazoe, T. Seiyama, Study of Metal Oxide Catalysts by Temperature Programmed Desorption. Oxygen Adsorption on Various Metal Oxides, J. Phys. Chem., 82 (1978) 2564-2570.
[62] M. Che, J.F.J. Kibblewhite, A.J. Tench, M. Dufaux, C. Naccache, Oxygen Species Adsorbed on CeO_2/SiO_2 Supported Catalysts, J. Chem. Soc., Faraday Trans. 1, 69 (1973) 857-863.
[63] T. Berger, O. Diwald, E. Knözinger, F. Napoli, M. Chiesa, E. Giamello, Hydrogen activation at TiO2 anatase nanocrystals, Chem. Phys., 339 (2007) 138-145.
[64] M.C. Paganini, D. Dalmasso, C. Gionco, V. Polliotto, L. Mantilleri, P. Calza, Beyond TiO2: Cerium-Doped Zinc Oxide as a New Photocatalyst for the Photodegradation of Persistent Pollutants, ChemistrySelect, 1 (2016) 3377-3383.
[65] F. Oba, A. Togo, I. Tanaka, J. Paier, G. Kresse, Defect energetics in ZnO: A hybrid Hartree-Fock density functional study, Phys. Rev. B, 77 (2008).
[66] F. Gallino, G. Pacchioni, C. Di Valentin, Transition levels of defect centers in ZnO by hybrid functionals and localized basis set approach, J. Chem. Phys., 133 (2010) 144512.
[67] C. Gionco, M.C. Paganini, E. Giamello, R. Burgess, C. Di Valentin, G. Pacchioni, Paramagnetic Defects in Polycrystalline Zirconia: An EPR and DFT Study, Chem. Mater., 25 (2013) 2243-2253.